A novel framework for estimating time-varying multivariate autoregressive models and application to cardiovascular responses to acute exercise

K. Kostoglou, A.D. Robertson, B. J. MacIntosh, G. D. Mitsis*

***Abstract*— *Objective:* We present a novel modeling framework for identifying time-varying (TV) couplings between time-series of biomedical relevance. *Methods:* The proposed methodology is based on multivariate autoregressive models (MVAR), which have been extensively used to study couplings between biosignals. Contrary to standard estimation methods that assume time-invariant relationships, we propose a modified recursive Kalman Filter (KF) to track changes in the model parameters. We perform model order selection and hyperparameter optimization simultaneously using Genetic Algorithms, greatly improving accuracy and computation time. In addition, we address the effect of residual heteroscedasticity, possibly associated with event-related changes or phase transitions during a given experimental protocol, on the TV-MVAR coupling measures by using Generalized Autoregressive Conditional Heteroskedasticity (GARCH) models to fit the TV-MVAR residuals. *Results:* Using simulated data, we show that the proposed framework yields more accurate parameter estimates compared to the conventional KF, particularly when the true system parameters exhibit different rate of variations over time. Furthermore, by accounting for heteroskedasticity, we obtain more accurate estimates of the strength and directionality of the underlying couplings. We also use our approach to investigate TV hemodynamic interactions during exercise in young and old healthy adults, as well as individuals with chronic stroke. We extract TV coupling patterns that reflect well known exercise-induced effects on the underlying regulatory mechanisms with excellent time resolution. *Conclusions and Significance:* The proposed modeling framework can be used to efficiently quantify TV couplings between biosignals. It is fully automated and does not require prior knowledge of the system TV characteristics.**

***Index Terms*—MVAR, time-varying, Kalman Filter, heteroskedasticity, partial directed coherence, exercise**

I. Introduction

Biological functions are often regulated by the coupling of individual oscillators. Oscillations have been identified, for example, as a fundamental property of neural responses [1], and couplings between different oscillatory neural populations are considered one of the most important mechanisms of information processing and communication between brain regions [2], [3]. Frequency-based characterization of information propagation under different brain states [4] and pathological conditions [5] has recently drawn growing attention. For instance, coherent oscillations between electroencephalography (EEG), electromyography (EMG) and magnetoencephalography (MEG) time-series have been increasingly used to elucidate the role of the motor cortex in movement control [6]. Furthermore, cardiovascular and respiratory system interactions and their directionality have been the subject of much research [7]–[9] since they can be used as biomarkers of impairment (e.g. baroreflex function or respiratory sinus arrhythmia impairment) in various cardiovascular and cardiorespiratory pathologies (e.g. heart failure, breathing disorders, neurally-mediated syncope).

Perhaps the most widely used method for characterizing such interactions is multivariate autoregressive (MVAR) modeling [10]. MVAR models have been successfully applied to various fields of biomedical research, including EEG/MEG-based cortical connectivity analysis [11]–[27] and detection of cardiovascular/cardiorespiratory couplings [9], [13], [36], [28]–[35]. MVAR models assume linear inter-dependencies among multiple time-series and have been used to assess causality in the time and frequency domains. However, the coupling strength and directionality between the time-series of interest may change through time. To address this, time-varying MVAR (TV-MVAR) models have been proposed. The main assumption in these models is that their parameters are no longer constant but vary as a function of time. TV-MVAR parameter estimation can be performed using recursive techniques, such as Recursive Least Squares (RLS) and the Kalman Filter (KF) [14]–[16], [18], [19], [21], [24], [26], [27], [30], which update the model parameters at each time step, yielding improved tracking resolution compared to quasistationary approaches [17], [20]. Recursive approaches usually rely on the optimal tuning of hyperparameters, e.g. the RLS forgetting factor that defines the memory of the estimator [37]. Furthermore, both the conventional KF and RLS assume a constant rate of variations, which is not always valid. Different model parameters may not change in the same manner; for instance, some may exhibit abrupt or fast variations while others may remain constant or evolve slowly through time. Thus, accurate quantification of TV interactions requires the development of algorithmic schemes that can track different types of possibly co-existing TV patterns. Furthermore, a crucial step is the selection of the MVAR model order, as incorrect model orders may severely deteriorate the resulting model time and frequency resolutions. In the TV case, model order selection presents additional challenges, as the underlying system characteristics vary over time (i.e. cross validation is not directly applicable). Finally, a major issue that may affect the accuracy of the coupling measures obtained from TV-MVAR models is heteroskedasticity of the residuals. Standard estimation

Manuscript received June 28, 2018; revised November 27, 2018, accepted February 20, 2019.

K. Kostoglou is with the Department of Electrical, Computer and Software Engineering, McGill University, Montreal, Canada.

A.D. Robertson is with the Canadian Partnership for Stroke Recovery, Sunnybrook Research Institute, University of Toronto, Toronto, Canada.

B. J. MacIntosh is with the Canadian Partnership for Stroke Recovery, Sunnybrook Research Institute and Department of Medical Biophysics, University of Toronto, Toronto, Canada.

*G. D. Mitsis is with the Department of Bioengineering, McGill University, Montreal, Canada (correspondence e-mail: georgios.mitsis@mcgill.ca).

methods assume normality in the error terms, with zero mean and constant variance (i.e. homoskedasticity) [10]. However, TV residual variances (heteroskedasticity) may arise due to changes in measurement noise, unobserved external factors or event-related changes and experimental phase transitions that are associated with different signal to noise ratio (SNR) levels. In turn, this may lead to inaccurate estimation of the strength and directionality of the underlying couplings.

To effectively address these issues, we have developed a novel recursive framework for estimating TV-MVAR models. This framework is based on the KF technique and can track accurately slow, fast or even mixed-mode variations combined with abrupt changes more efficiently by assuming that each model parameter follows a random walk driven by Gaussian white noise (GWN) with unique TV variance. Model order selection and hyperparameter optimization were simultaneously performed using Genetic Algorithms (GA), which offers significant advantages compared to exhaustive search procedures. In addition, we implemented schemes that mitigate the effects of heteroskedasticity on the accuracy of the TV-MVAR coupling measures. The improved performance of the proposed framework was assessed using simulations. Finally, we applied the proposed framework to investigate cerebrovascular regulation during exercise in healthy subjects and stroke survivors.

II. Methods

A. Time-varying Multivariate Autoregressive (TV-MVAR) Models

In MVAR models, each variable of interest depends linearly on its past values and the past values of all other variables [10]. Under the assumption of time-invariance, the dynamic effects of each time-series on itself and all other time-series are constant throughout time. On the other hand, a TV-MVAR model of order p is given by [15]–[18], [20], [27], [38], [39],

$$\boldsymbol{y}(n) = \sum_{k=1}^{p} \boldsymbol{A}_k(n)\boldsymbol{y}(n-k) + \boldsymbol{\varepsilon}(n) = \boldsymbol{A}(n)\boldsymbol{\Phi}(n) + \boldsymbol{\varepsilon}(n) \quad (1)$$

where $\boldsymbol{y}(n) \in \boldsymbol{R}^{M\times 1}$ is a vector of M time-series at time n, $\boldsymbol{A}_k(n) \in \boldsymbol{R}^{M\times M}$ is a TV autoregressive matrix for each order k, $\boldsymbol{A}(n) = [\boldsymbol{A_1}(n) \quad \dots \quad \boldsymbol{A}_p(n)] \in \boldsymbol{R}^{M\times Mp}$, $\boldsymbol{\Phi}(n) = [\boldsymbol{y}(n-1) \quad \dots \quad \boldsymbol{y}(n-p)]^{\boldsymbol{T}} \in \boldsymbol{R}^{Mp\times 1}$ and $\boldsymbol{\varepsilon}(n)$ is assumed to be a zero-mean white noise vector. $\boldsymbol{A}_k(n)$ depends explicitly on time n, in contrast to standard MVAR models. To facilitate parameter estimation, we reformulate (1) as,

$$\boldsymbol{y}(n) = [\boldsymbol{I}_{M\times M} \otimes \boldsymbol{\Phi^T}(n)]\,\boldsymbol{\Gamma}(n) + \boldsymbol{\varepsilon}(n) \Rightarrow$$
$$\boldsymbol{y}(n) = \widetilde{\boldsymbol{\Phi}}(n)\boldsymbol{\Gamma}(n) + \boldsymbol{\varepsilon}(n) \quad (2)$$

where $\boldsymbol{I}_{M\times M}$ is the identity matrix, $\otimes$ denotes the Kronecker delta product, $\widetilde{\boldsymbol{\Phi}}(n) = \boldsymbol{I}_{M\times M} \otimes \boldsymbol{\Phi^T}(n) \in \boldsymbol{R}^{M\times M^2 p}$ is an extended regressor matrix and $\boldsymbol{\Gamma}(n) \in \boldsymbol{R}^{M^2 p\times 1}$ is the vectorized $\boldsymbol{A}(n)$ containing all MVAR parameters at time n.

B. TV-MVAR Parameter Estimation

The conventional KF assumes that parameter changes are modeled as a random walk driven by GWN with covariance equal to $\boldsymbol{R_1} = R_1\boldsymbol{I}_{d\times d}$. In effect, R_1 defines the size of the expected parameter variations. The KF is based on the hypothesis that the measurement noise is also GWN with variance R_2. The KF combined with the MVAR formulation presented in (2) consists of the following recursive steps [15], [16], [18], [27], [38], [39],

$$\boldsymbol{e}(n) = \boldsymbol{y}(n) - \hat{\boldsymbol{y}}(n) = \widetilde{\boldsymbol{\Phi}}(n)\hat{\boldsymbol{\Gamma}}(n-1) \quad (3)$$

$$\boldsymbol{r}(n) = \widetilde{\boldsymbol{\Phi}}(n)\boldsymbol{P}(n-1)\widetilde{\boldsymbol{\Phi}}(n) \quad (4)$$

$$\boldsymbol{K}(n) = \frac{\boldsymbol{P}(n-1)\widetilde{\boldsymbol{\Phi}}^{\boldsymbol{T}}(n)}{R_2 + \boldsymbol{r}(n)} \quad (5)$$

$$\boldsymbol{P}(n) = \boldsymbol{P}(n-1) + \boldsymbol{R_1} - \boldsymbol{K}(n)\widetilde{\boldsymbol{\Phi}}(n)\boldsymbol{P}(n-1) \quad (6)$$

$$\hat{\boldsymbol{\Gamma}}(n) = \hat{\boldsymbol{\Gamma}}(n-1) + \boldsymbol{K}(n)\boldsymbol{e}(n) \quad (7)$$

where $\hat{\boldsymbol{\Gamma}}(n) \in \boldsymbol{R}^{d\times 1}$ are the estimated parameters at time n, $d = M^2 p$ is the total number of parameters, $\boldsymbol{P}(n) \in \boldsymbol{R}^{d\times d}$ is the parameter estimation error covariance with initial value $\boldsymbol{P_0} = P_0 I_{d\times d}$, $\boldsymbol{K}(n) \in \boldsymbol{R}^{d\times M}$ is the Kalman gain, R_2 is the measurement noise variance and $\boldsymbol{R_1} \in \boldsymbol{R}^{d\times d}$ is the diagonal process noise covariance.

In cases where the parameters vary with different rates, the conventional KF formulation is not optimal. Parameters that exhibit large and fast variations should be assigned with larger R_1 values compared to those that exhibit slow and small changes. Moreover, the underlying TV patterns may not be periodic and may be characterized by a mixture of slow, fast and abrupt variations. To address this, we propose updating the diagonal process noise covariance matrix $\boldsymbol{R_1}$ adaptively at each time step as follows,

$$\boldsymbol{R_1}(n) = \boldsymbol{\Lambda_w}\boldsymbol{R_1}(n-1) + (\boldsymbol{I} - \boldsymbol{\Lambda_w})e^2(n) \quad (8)$$

$$\boldsymbol{\Lambda_w} = diag\{\boldsymbol{\lambda_w}\}, \qquad \boldsymbol{\lambda_w} = [\lambda_{w_1} \quad \dots \quad \lambda_{w_d}] \quad (9)$$

where $\boldsymbol{\Lambda_w} \in \boldsymbol{R}^{d\times d}$ is a diagonal matrix of smoothing factors λ_{w_j} for $j = 1 \dots d$, which lie between 0 and 1. The rationale behind (8) and (9) is that changes in the parameters can be detected by tracking the variations of the error terms. Equation (8) can be described as a multivariate moving average that follows the mean of the variance of the residuals with different rates. Through (8) and (9), we are assigning unique adaptive update coefficients to each model parameter. In addition, we assume that the noise measurement variance is different for each time-series and therefore R_2 in (5) becomes a diagonal, M-dimensional matrix $\boldsymbol{R_2} = diag\{\boldsymbol{r_2}\}$, $\boldsymbol{r_2} = [r_{2_1} \quad \dots \quad r_{2_M}]$.

C. Model Order Selection and Parameter Optimization

Model order selection and optimization of the hyperparameters $\boldsymbol{\lambda_w}$, $\boldsymbol{r_2}$ and P_0 is realized using a mixed integer Genetic Algorithm (GA) [40]–[42]. GAs can be described as adaptive search algorithms inspired from natural evolution. In each generation, the fitness function of a population of candidate solutions is evaluated. The fittest solutions are then selected and used in the next iteration of the algorithm. The candidate solutions $\boldsymbol{X}_i$ are of the form,

$$\boldsymbol{X}_i = [p \quad \boldsymbol{\lambda_w} \quad \boldsymbol{r_2} \quad P_0] \quad (10)$$

where $p \in [1 \dots p_{max}]$ is the selected model order and p_{max} is the maximum considered order. Each element of $\boldsymbol{\lambda_w}$ lies between 0 and 1, whereas P_0 and the elements of $\boldsymbol{r_2}$ are constrained to positive values. The total number of hyperparameters optimized by the GA is $2 + M^2 p + M$. For the conventional KF, the tunable hyperparameters are R_1, R_2 and P_0. Thus, the candidate solutions assume the form,

$$\boldsymbol{X}_i = [p \quad R_1 \quad R_2 \quad P_0] \tag{11}$$

We select the Akaike Information Criterion (AIC) [43] on the entire dataset as the fitness function, as it accounts for both the prediction error and the total number of model parameters and has been used extensively for many model types, including TV-MVAR models [16], [44]. Thus, for each $\boldsymbol{X}_i$, the GA recursively estimates the model based on all the available data and computes the following quantity [45], [46],

$$AIC(\boldsymbol{X}_i) = N\log\left(|\widehat{\boldsymbol{\Sigma}}|\right) + 2d \tag{12}$$

where N is the length of the dataset, $d = M^2p$ is the total number of parameters and $|\widehat{\boldsymbol{\Sigma}}|$ is the determinant of the estimated error covariance, i.e. $\widehat{\boldsymbol{\Sigma}} = cov\left(\boldsymbol{Y} - \widehat{\boldsymbol{Y}}\right) = cov(\boldsymbol{e})$. The optimal solution is the one with the lowest AIC score.

D. Smoothing

Smoothing is subsequently applied to the extracted TV model parameters in order to deal with noisy estimates either due to fast adaptation or excessive noise. Specifically, we use the Rauch-Tung-Striebel [47], [48] fixed-interval equations,

$$\boldsymbol{W}(n) = \boldsymbol{P}(n)[\boldsymbol{P}(n+1) + \boldsymbol{R_1}(n+1)]^{-1} \tag{13}$$

$$\widehat{\boldsymbol{\Gamma}}^{\boldsymbol{s}}(n) = \widehat{\boldsymbol{\Gamma}}(n) + \boldsymbol{W}(n)\left[\widehat{\boldsymbol{\Gamma}}^{\boldsymbol{s}}(n+1) - \widehat{\boldsymbol{\Gamma}}(n)\right] \tag{14}$$

By applying (14) and updating $\widehat{\boldsymbol{\Gamma}}(n)$ in a backward manner starting from time point $n = N-1$ up to $n = 1$ with initial values $\widehat{\boldsymbol{\Gamma}}^{\boldsymbol{s}}(N) = \widehat{\boldsymbol{\Gamma}}(N)$, the smoothed estimates $\widehat{\boldsymbol{\Gamma}}^{\boldsymbol{s}}$ are obtained. The matrices $\boldsymbol{P}(n)$ and $\boldsymbol{R_1}(n)$ in (13) are computed during the forward sweep (6,8-9).

E. TV-MVAR Measures of Coupling and Causality

By taking the Fourier transform (FT) of (1), the TV *spectral power density matrix* of $\boldsymbol{y}$ can be computed as,

$$\boldsymbol{S}(f,n) = \boldsymbol{H}(f,n)\boldsymbol{\Sigma}\boldsymbol{H}^H(f,n) \tag{15}$$

where $\boldsymbol{H}(f,n) = [\boldsymbol{I} - \boldsymbol{A}(f,n)]^{-1} = \overline{\boldsymbol{A}}(f,n)^{-1} \in \boldsymbol{R}^{M\times M}$ is the TV *transfer matrix* in the frequency domain at time point n, $\boldsymbol{A}(f,n) = \sum_{k=1}^{\boldsymbol{p}} \boldsymbol{A_k}(n)e^{-i2\pi fkT}$ is the TV *coefficient matrix* and $\boldsymbol{\Sigma} = diag([\sigma_1^2 \ldots \sigma_M^2]) \in \boldsymbol{R}^{M\times M}$ is the diagonal covariance matrix of $\boldsymbol{\varepsilon}$. The superscript *H* stands for Hermitian transpose. Similarly, the TV *inverse spectral power density matrix* of $\boldsymbol{y}$ is

$$\boldsymbol{P}(f,n) = \boldsymbol{S}^{-1}(f,n) = \overline{\boldsymbol{A}}^H(f,n)\boldsymbol{\Sigma}^{-1}\overline{\boldsymbol{A}}(f,n) \tag{16}$$

The elements of the TV spectral density, transfer function, and coefficient matrices can be used to assess TV couplings and causality in the frequency domain. Specifically,

$$COH_{TD}(f,n) = \frac{S_{TD}(f,n)}{\sqrt{S_{TT}(f,n)}\sqrt{S_{DD}(f,n)}} \tag{17}$$

$$DC_{TD}(f,n) = \frac{\sigma_D H_{TD}(f,n)}{\sqrt{\sum_{m=1}^{M}\sigma_m^2|H_{Tm}(f,n)|^2}} \tag{18}$$

$$PCOH_{TD}(f,n) = \frac{P_{TD}(f,n)}{\sqrt{P_{TT}(f,n)}\sqrt{P_{DD}(f,n)}} \tag{19}$$

$$GPDC_{TD}(f,n) = \frac{\frac{1}{\sigma_T}\bar{A}_{TD}(f,n)}{\sqrt{\sum_{m=1}^{M}\frac{1}{\sigma_m^2}|\bar{A}_{mD}(f,n)|^2}} \tag{20}$$

where COH_{TD} describes the *Coherence* from D (driver) to T (target) [49], DC_{TD} the *Directed Coherence* [50], $PCOH_{TD}$ the *Partial Coherence* [51], [52] and $GPDC_{TD}$ the *Generalized Partial Directed Coherence* [53]. The coupling measures of (17)-(20) are complex-valued and thus their squared modulus is commonly used. All these squared measures take values between 0 and 1. COH quantifies the linear coupling strength between two processes in the frequency domain, whereas $PCOH$ differentiates direct from indirect connections. COH and $PCOH$ are symmetric, non-directional measures that can be decomposed into subcomponents that quantify directionality (DC and $GPDC$ respectively). DC quantifies the direct and indirect causal links between two time-series, while $GPDC$ quantifies direct causal influences only, without considering indirect paths of information flow. Since $\boldsymbol{\Sigma}$ is unknown in practice, an estimate $\widehat{\boldsymbol{\Sigma}}$ is obtained from the model residuals ($\widehat{\boldsymbol{\Sigma}} = cov\left(\boldsymbol{Y} - \widehat{\boldsymbol{Y}}\right) = cov(\boldsymbol{e})$). Thus, the elements of $\boldsymbol{\Sigma}$ in (15)-(20) are substituted by the elements of $\widehat{\boldsymbol{\Sigma}}$.

F. Heteroskedasticity in the error terms

TV-MVAR estimation is typically based on the assumption that the residuals are white, with zero mean and constant variance (homoskedastic). However, model residuals may exhibit TV variance. Ignoring heteroskedasticity may lead to inaccurate error covariance estimates ($\widehat{\boldsymbol{\Sigma}}$), which may in turn bias the coupling measures extracted from the TV-MVAR models (17)-(20). In practice, the covariance matrix $\widehat{\boldsymbol{\Sigma}}$ is estimated either based on the residuals acquired from the entire dataset [18], [44] or by segmenting into windows [17]. In recursive approaches, these windows are comparable in size with the recursive estimator's memory [16], [39]. However, heteroskedasticity implies that $\boldsymbol{\Sigma}$ is TV in nature and does not necessarily follow the same TV patterns as the model parameters. Hence, after estimating the TV model parameters and extracting the model residuals, we propose tracking the TV $\widehat{\boldsymbol{\Sigma}}(n)$ using Generalized Autoregressive Conditional Heteroskedasticity (GARCH) models [54]. GARCH models can be used to describe time-series with changing, possibly volatile variance [54]. Under heteroskedasticity, the variance of each error term is a function of time,

$$\varepsilon_m(n) \sim N(0, \sigma_m^2(n)) \qquad for\ m = 1 \ldots M \tag{21}$$

A GARCH model of order (r,q) expresses the current conditional variance as a linear combination of past conditional variances and squared errors,

$$\sigma_m^2(n) = \omega_m + \sum_{i=1}^{r}\gamma_{im}\varepsilon_m^2(n-i) + \sum_{j=1}^{q}\delta_{jm}\sigma_m^2(t-j) \tag{22}$$

The optimal model order (r,q) is selected based on the AIC criterion [43]. Finally, the time-invariant estimate of the error covariance $\widehat{\boldsymbol{\Sigma}}$ can be replaced at each time point with the TV covariance $\widehat{\boldsymbol{\Sigma}}(n)$ obtained by the GARCH model (22).

III. Simulations

We generated 50 realizations of the following 3-dimensional TV-MVAR process of order 2 ($M = 3$; $p = 2$),

$$\begin{bmatrix} y_1(n) \\ y_2(n) \\ y_3(n) \end{bmatrix} = \sum_{k=1}^{2}\boldsymbol{A}_k(n)\begin{bmatrix} y_1(n-k) \\ y_2(n-k) \\ y_3(n-k) \end{bmatrix} + \begin{bmatrix} \varepsilon_1(n) \\ \varepsilon_2(n) \\ \varepsilon_3(n) \end{bmatrix} \tag{23}$$

$$\boldsymbol{A}_k(n) = \begin{bmatrix} a_{11}^{(k)}(n) & a_{12}^{(k)}(n) & a_{13}^{(k)}(n) \\ a_{21}^{(k)}(n) & a_{22}^{(k)}(n) & a_{23}^{(k)}(n) \\ a_{31}^{(k)}(n) & a_{32}^{(k)}(n) & a_{33}^{(k)}(n) \end{bmatrix} \quad (24)$$

TV couplings were implemented by varying the model parameters ($\boldsymbol{A}_k$) through time as depicted in Fig. 1a. The TV-MVAR process was driven by Gaussian white homoskedastic or heteroskedastic noise (sections III.A and B respectively). The mean and standard deviation of the simulated time-series over all 50 realizations, as well as representative realizations can be found in the Supplementary Material (Figs. S1, S4).

TV parameter estimation was performed using the conventional (3)-(7) and proposed KF implementation (3)-(9). Model order and hyperparameter optimization was performed in both cases using the GA (Section II.C). The performance of the two estimators was assessed by computing the mean squared error (MSE) between actual and estimated parameters,

$$MSE = \frac{1}{Nd}\sum_{j=1}^{d}\sum_{n=1}^{N}\left[\Gamma_j(n) - \hat{\Gamma}_j(n)\right]^2 \quad (25)$$

where $\Gamma_j(n)$ is the j-th element of the true parameter vector $\boldsymbol{\Gamma}$ at time n, while $\hat{\Gamma}_j(n)$ corresponds to the j-th element of the estimated unsmoothed parameter vector at time n. When smoothing was applied, $\hat{\Gamma}_j(n)$ was replaced with its smoothed version $\hat{\Gamma}_j^s(n)$ (14). We also estimated the normalized MSE (NMSE) between true and estimated measures of (15)-(20),

$$NMSE(\%) = \frac{100}{M^2}\sum_{T=1}^{M}\sum_{D=1}^{M}\left\{\frac{\sum_{n=1}^{N}\sum_f\left[Z_{TD}(f,n) - \hat{Z}_{TD}(f,n)\right]^2}{\sum_{n=1}^{N}\sum_f\left[Z_{TD}(f,n)\right]^2}\right\} \quad (26)$$

where $Z_{TD}(f,n)$ and $\hat{Z}_{TD}(f,n)$ refer to the true and estimated TV-MVAR measures (15-20), respectively.

A. *Case 1: Homoskedastic error terms*

The TV-MVAR process of (23) was driven by GWN signals $\boldsymbol{\varepsilon}$ of equal variances,

$$\boldsymbol{\Sigma} = \begin{bmatrix} \sigma_1^2 & 0 & 0 \\ 0 & \sigma_2^2 & 0 \\ 0 & 0 & \sigma_3^2 \end{bmatrix} = \begin{bmatrix} \sigma^2 & 0 & 0 \\ 0 & \sigma^2 & 0 \\ 0 & 0 & \sigma^2 \end{bmatrix} = \begin{bmatrix} 1 & 0 & 0 \\ 0 & 1 & 0 \\ 0 & 0 & 1 \end{bmatrix} \quad (27)$$

The GA identified the correct model order in all cases. Note that in additional simulations, where the true order p was set to 4 and 6, we found that the GA yielded the correct order in the vast majority of cases. The GA optimization technique has been used in a previous study related to FIR nonlinear (Laguerre-Volterra) models [42]. In that study, we provide a more extensive analysis regarding the model order selection procedure, as well as results from multiple simulations. The main related conclusions of that study can be extended to the MVAR models examined here. As shown in Fig. 1b (left panel - Homoskedasticity), our approach yielded significantly lower MSE values compared to the conventional KF (both with/without smoothing) indicating superior tracking performance. In Fig. 2, we show the true and estimated TV COH (averaged over all 50 realizations) from our implementation combined with smoothing. The true and estimated TV parameters, as well as the resulting TV patterns for all MVAR measures can be found in the Supplementary Material (Figs. S2, S3). The proposed framework captured accurately changes in coupling strength and directionality. TV COH was computed using (17). $\hat{\boldsymbol{\Sigma}}$ was estimated using the residuals obtained from the entire dataset. The required computation time for GA optimization and parameter estimation was 5.36±0.68 and 34.43±0.68 seconds using the conventional and proposed KF respectively (Intel Core i7-7500U@2.70GHz, 16GB RAM using Matlab MEX functions and parallel computing. The Matlab code implementation of the TV-MVAR modeling framework can be found at https://codeocean.com/capsule/4783581). On the other hand, applying the conventional KF and grid search with a coarse grid ($p = 1{:}10, R_2 = 1, R_1$ and $P_0 = 50$ logarithmically spaced points between 10^{-4} and 10^3), the runtime was 117.84 seconds. Implementing grid search to achieve similar grid resolution to our proposed approach, which based on (10) requires $2 + M^2p + M$ function evaluations, would lead to a runtime of hours.

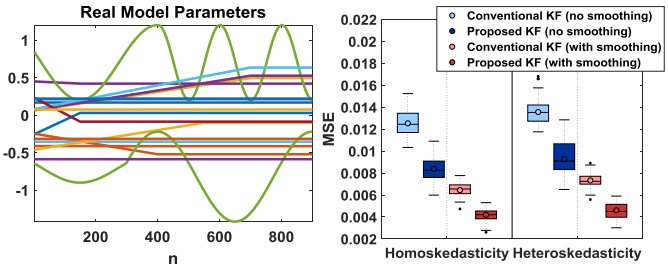

Figure 1: Simulated data - (a) True TV model parameters of the TV-MVAR process of (23) and (24). The parameters either remain constant throughout time or evolve as ramps or sinusoids with TV amplitude and frequency (b) Boxplots of the MSE values obtained between true and estimated parameters over all 50 realizations, before and after applying smoothing, using the conventional and proposed KF implementation under both homoskedastic (Case 1) and heteroskedastic error terms (Case 2). Statistically significant differences were assessed using analysis of variance (ANOVA) with Tukey's honestly significant difference test post hoc. All post hoc comparisons were significant (p<3.7E-09) for each Case separately. The mean and standard deviation for each estimated parameter as a function of time can be found in the Supplementary Material (Figs. S2 and S5).

B. *Case 2: Heteroskedastic error terms*

Here, the variance of the driving GWN signals of the TV-MVAR process of (23) was changed over time as follows,

$$\boldsymbol{\Sigma_1} = \begin{bmatrix} 1 & 0 & 0 \\ 0 & 1 & 0 \\ 0 & 0 & 1 \end{bmatrix} \quad for\ n \le 450 \quad (28)$$

$$\boldsymbol{\Sigma_2} = \begin{bmatrix} 0.5 & 0 & 0 \\ 0 & 0.8 & 0 \\ 0 & 0 & 0.2 \end{bmatrix} \quad for\ n > 450 \quad (29)$$

The proposed implementation with and without smoothing yielded significantly better performance compared to the conventional KF (Fig.1b; right panel – Heteroskedasticity). The true and estimated TV parameters can be found in the Supplementary Material (Fig.S5). We observed that the TV variance of the error terms led to slightly higher MSE values between true and estimated parameters compared to Case 1. The proposed KF approach was affected less by the induced heteroskedasticity and exhibited a more robust behavior compared to the conventional KF.

To take into account heteroskedasticity, we parametrized the TV $\hat{\boldsymbol{\Sigma}}$ using the GARCH approach described in Section

This article has been accepted for publication in a future issue of this journal, but has not been fully edited. Content may change prior to final publication. Citation information: DOI 10.1109/TBME.2019.2903012, IEEE Transactions on Biomedical Engineering

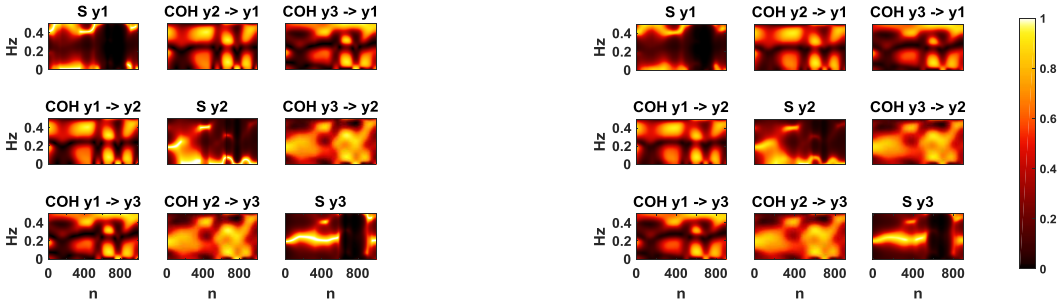

Figure 2: Simulation study, Case 1 - (a) true and (b) estimated TV COH under homoskedastic error terms using our proposed algorithm combined with smoothing (average from all 50 realizations). The x and y axes represent time and frequency respectively. $y_D \rightarrow y_T$ denotes the driver and target time-series. COH is a symmetric, non-directional measure that reflects direct and indirect couplings between two time-series. Thus, COH $y_D \rightarrow y_T$ is equal to COH $y_T \rightarrow y_D$. The diagonal components of COH are the spectra (S) of each time-series. The colormap of the figure was designed by Peter Kovesi [55].

II.F. Fig. 3 illustrates the average and standard deviation (over all 50 realizations) of the estimated TV error term variance for all three time-series using both the conventional and proposed KF. The GARCH models were successful in tracking changes in the variance of the error terms. Furthermore, our proposed approach led to less biased estimates of the variance.

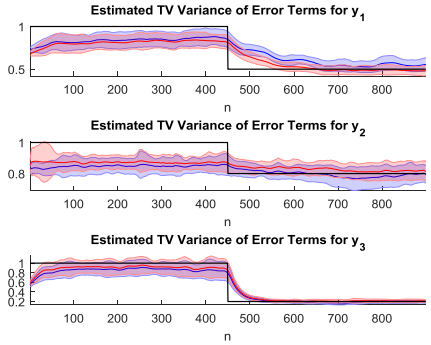

Figure 3: Mean±std (over all 50 realizations) of the estimated TV variance of the error terms for all three time-series based on the GARCH approach using the conventional (blue) and proposed (red) KF. The black lines denote the true changes in the variance of the error terms. The proposed KF leads to less biased estimates of the TV variance. Note that for the second time-series y_2, the change in variance is not as easily detectable as the two other time-series due to the relatively small size of the amplitude step change.

TV-MVAR measures were computed based on (15)-(20) combined with (22). In Fig. 4 we show the obtained NMSE(%) from Case 2 using the conventional and proposed KF with smoothing, when heteroskedasticity was ignored (i.e. estimating $\widehat{\boldsymbol{\Sigma}}$ based on the residuals of the entire dataset**)** or taken into account (i.e. tracking $\widehat{\boldsymbol{\Sigma}}$ using GARCH models). Accounting for heteroskedasticity with the proposed GARCH approach resulted in lower NMSE(%) for all TV-MVAR estimates, using both the conventional KF and the proposed approach, with the latter outperforming the former in all cases (Fig. 4b). Fig. 5 illustrates the true and estimated TV $GPDC$ between all three time-series. The true and estimated TV-MVAR measures can be found in the Supplementary Material (Fig. S6). When heteroskedasticity was ignored, $GPDC$ was either overestimated or underestimated within specific time intervals (Fig. 5b), possibly leading to erroneous conclusions. For example, Fig. 5b suggests a larger flow of information from y_3 to y_2 within [0.2 0.3Hz] after time point 450 whereas, the true causality strength between these two time-series was higher before that time point (Fig. 5a). This was not the case when applying the proposed GARCH approach (Fig. 5c).

IV. Experimental Data

A. Experimental Protocol and Data Preprocessing

Growing evidence suggests that even a single exercise session elicits changes in cerebrovascular function in healthy adults and patients with stroke [56]–[58]. To quantify the interaction of cardiovascular and cerebrovascular signals during physical activity, we applied the proposed TV-MVAR methodology using stroke volume (SV), pulse pressure (PP), and middle cerebral artery pulsatility index (PI) time-series collected during exercise. SV is the volume of blood pumped through the left heart ventricle with each contraction. PP describes the differential in arterial blood pressure between the systolic and diastolic phases of the cardiac cycle and PI reflects the intra-beat pulsatile characteristics of cerebral blood flow velocity. The ratio SV/PP is regarded as a simplified index of arterial compliance [59] and has been proposed as a biomarker of cardiovascular risk [60]. A number of studies have shown that physical activity can lead to short- and long-term increases in arterial compliance, reducing the negative effects of arterial stiffness [61]–[66]. On the other hand, PP and PI are linked to cerebral autoregulation [67], a mechanism that maintains blood flow to the brain constant despite variations in arterial blood pressure. Our main aim was to track TV changes in both arterial compliance and cerebral autoregulation during and after exercise. To this end, participants from 3 groups [stroke survivors (n=17), young (n=12) and elderly healthy adults (n=10)] performed 20 min of moderate intensity stationary cycling. The experimental protocol consisted of the following six phases,

Phase 1*:* 5 min of seated rest.
Phase 2*:* 3 min warm-up; increasing workload each min.
Phase 3*:* 20 min of steady-state exercise.
Phase 4*:* 2 min cool-down; decreasing workload each min.
Phase 5*:* 1 min cool-down in cycling position; no pedaling.
Phase 6*:* 5 min post-exercise seated recovery.

The experimental protocol was approved by the Sunnybrook Health Sciences Centre and University Health Network research ethics boards. All participants provided written informed consent.

No preprocessing was applied to the data except for adding a constant offset vector to (1) that was optimized by the GA along with the remaining hyperparameters (10). The residuals were found to be heteroskedastic by applying normality tests and examining parameter significance when fitting GARCH

This article has been accepted for publication in a future issue of this journal, but has not been fully edited. Content may change prior to final publication. Citation information: DOI 10.1109/TBME.2019.2903012, IEEE Transactions on Biomedical Engineering

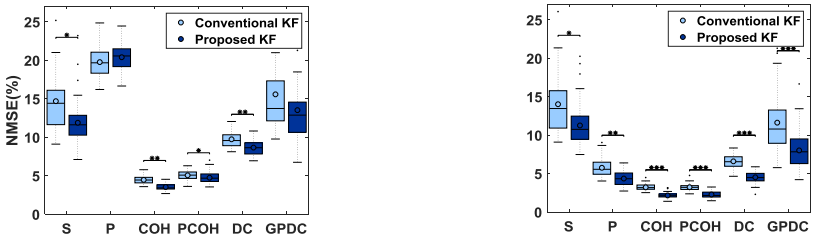

Figure 4: Simulation study, Case 2 - Boxplots depicting the NMSE(%) between true and estimated TV-MVAR measures (i.e. $S, P, COH, PCOH, DC, GPDC$ in (15)-(20)) using the conventional KF (light blue) and the proposed algorithm (dark blue) under heteroskedastic error terms, whereby heteroskedasticity was (a) ignored (b) taken into account. Asterisks denote statistically significant differences between the conventional KF and the proposed approach (paired *t*-tests): *p≤0.02, **p≤2.85E-07, ***p≤4.29E-16. Taking account heteroskedasticity resulted in more accurate estimates of the TV-MVAR measures of (15)-(20). Moreover, the proposed algorithm resulted in significantly lower NMSE(%) values compared to the conventional KF. The figure was created based on the Matlab scripts found in the following link: http://alex.bikfalvi.com/research/advanced_matlab_boxplot

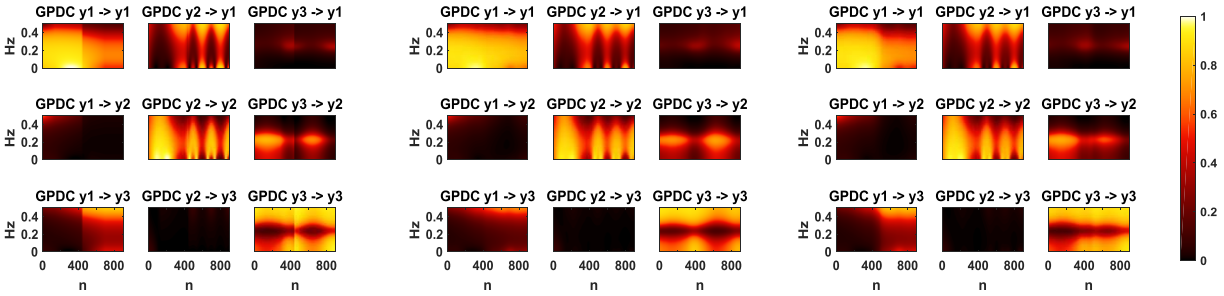

Figure 5: Simulation study, Case 2 – (a) true and (b) estimated TV $GPDC$ using our proposed implementation ignoring heteroskedasticity and (c) estimated TV $GPDC$ using our proposed implementation taking into account heteroskedasticity (average from all 50 realizations). The x and y axes represent time and frequency respectively. $y_D \rightarrow y_T$ denotes the driver and the target. $GPDC$ is an asymmetric measure that quantifies direct causality strength between two time-series. Thus, $GPDC$ $y_D \rightarrow y_T$ is not the same as $GPDC$ $y_T \rightarrow y_D$. The variance of the driving noise changes at time point 450. (c) approximates (a) more accurately than (b). For example, (b) suggests a larger flow of information from y_3 to y_2 within [0.2 0.3Hz] after time point 450, whereas the true causality strength between these two time-series is higher before that time point. This is captured when applying the proposed GARCH approach in (c).

models on the residuals) associated with experimental phase transitions (Supplementary Material – Fig. S8). Thus, we applied the GARCH approach (Section II.F) to quantify the changing variance of the error terms. For each group (healthy young and elderly, stroke survivors), we computed the resulting median TV COH, $PCOH$, DC and PDC (Fig. 6 and Fig. S7 in the Supplementary Material). The observed differences between the proposed approach and the conventional KF without tracking the TV variance of the residuals can be seen in Fig. 7, as well as Fig. S9 in the Supplementary Material. Ignoring heteroskedasticity led to over/underestimating the coupling strength in specific frequency bands, especially during the baseline and recovery phases. We focused on three bands of interest: very low (VLF; 0.01-0.04Hz), low (LF; 0.04-0.2Hz) and high (HF; 0.2-0.35Hz). To perform statistical comparisons between coupling measures during different phases, we extracted bandlimited mean values over all participants for each TV measure during baseline (Phase 1), exercise (Phase 3) and post-exercise recovery (Phase 6) (Supplementary Material - Fig. S10).

B. Results and Discussion

All groups exhibited the same hemodynamic profile; a progressive dissociation between SV and PP after the onset of exercise and a return to baseline or higher than baseline values during post-exercise recovery (Fig. 6a,b,c). The loss of coherence between SV and PP is in accordance with previous studies that have reported exercise-induced decreases in the SV/PP ratio [68], as well as the coherence between SV and systolic blood pressure [69]. This implies that arterial stiffness increases during exercise, reflecting the fact that exercise stress activates the sympathetic nervous system [70]. Specifically sympathetic activation leads to arterial blood pressure and heart rate increases [71], which temporarily induce vasoconstriction and arterial stiffening. Fig. 7a,b,c shows a gradual decrease in COH from young to elderly to stroke survivors. This is expected since the SV/PP ratio is an indirect measure of arterial compliance, which is known to decrease with age and by stroke occurrence [72], [73].

DC revealed that the main directionality effects occurred from SV to PP (Supplementary Material – Fig. S7), indicating that changes in SV lead to changes in PP, as is physiologically expected [74]. Based on the obtained $GPDC$ estimates, direct TV effects from SV to PP in the young group were more pronounced in the HF range (Fig. 6d,e,f), particularly between 0.25-0.35Hz. On the other hand, in the elderly and stroke survivors, SV directly affected PP more strongly in the LF range (Fig. 6d,e,f). Interactions within the LF and HF range may represent two distinct mechanisms, with the HF component being more active in the younger subjects. Cardiovascular signal spectral signatures within the LF and HF range have been associated with sympathetic and parasympathetic activity, respectively [75], [76]. Physiological ageing and stroke are linked with autonomic dysregulation and, specifically, a reduction in parasympathetic control and increase in sympathetic tone [77]–[79]. This could explain the low HF $GPDC_{\mathrm{SV->PP}}$ component during baseline in the healthy elderly and stroke groups (Fig. 6e,f). Both the elderly and stroke survivors exhibited increases in LF and HF $GPDC$

This article has been accepted for publication in a future issue of this journal, but has not been fully edited. Content may change prior to final publication. Citation information: DOI 10.1109/TBME.2019.2903012, IEEE Transactions on Biomedical Engineering

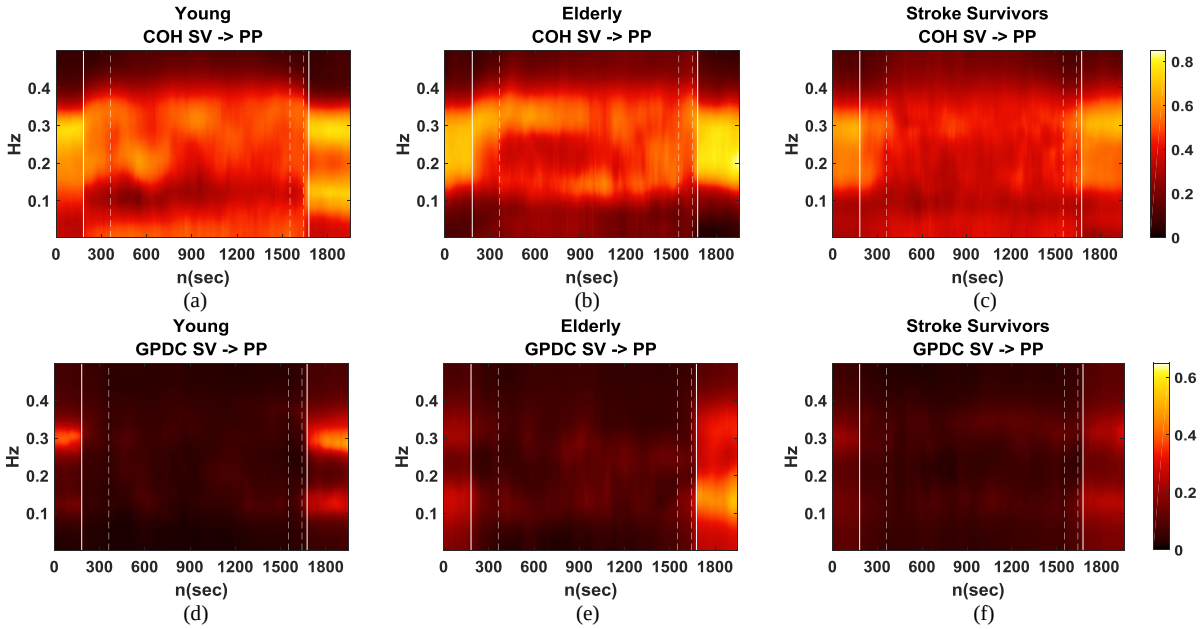

Figure 6: Median (a,b,c) TV COH between SV and PP and (d,e,f) TV $GPDC$ from SV to PP obtained from (a,d) healthy young, (b,e) healthy elderly and (c,f) stroke survivors respectively. The solid white lines denote the onset and offset of the cycling phase (onset of Phases 2 and 6). Dashed white lines denote transition phases. All groups exhibited the same hemodynamic profile; a progressive dissociation between SV and PP after the onset of exercise and a return to baseline or higher than baseline values during post-exercise recovery. A gradual decrease in COH values from young to elderly to stroke survivors was also observed. Direct TV effects from SV to PP in the young group were more pronounced in the HF range. On the other hand, in the elderly and stroke survivors, SV directly affected PP more strongly in the LF range.

from baseline during recovery, indicating probable increases in both sympathetic and parasympathetic activity. This implies that exercise may be promoting partial restoration of parasympathetic tone that is lost post-stroke and with age. Note that COH describes both the direct and indirect influences on the SV-PP relationship. However, $GPDC$ quantifies the directional influence of one signal on the other and may thus reflect different regulatory actions.

No significant exercise-related changes were found in associations between PI and SV or PP (Supplementary Material – Fig. S7). The relationship between PI and the remaining signals was mostly stationary and more prominent in the VLF/LF range. PP and PI are linked to cerebral autoregulation [67]. Based on transfer function analysis, it has been previously shown that autoregulation is maintained during low and moderate intensity exercise in the LF range [80]. This has also been demonstrated in healthy aging [81].

The main differences in the estimated TV $GPDC$ and COH using the conventional KF without taking into account heteroskedasticity and the proposed KF combined with the GARCH approach are summarized in Fig.7. Using the conventional KF without the GARCH approach led to an overestimation of COH between SV and PP in the LF band during exercise and in the HF band during recovery in all groups. $GPDC$ from SV to PP was consistently overestimated mainly around 0.1 and 0.2Hz and underestimated around 0.15 and 0.25Hz during baseline and recovery.

V. Conclusion

We introduced a novel TV-MVAR methodology that can be used to track time-varying interactions between multiple biosignals with high accuracy. The proposed approach is based on the KF technique, which was modified to accommodate multiple adaptive update coefficients, allowing independent tracking of each model parameter. A mixed integer GA was used to simultaneously select the optimal model order and tune the hyperparameters of the proposed recursive scheme, thus avoiding exhaustive search procedures. Heteroskedasticity in the error terms was parametrized using GARCH models. Based on simulations, our approach achieved superior performance compared to the conventional KF and led to more accurate representations of the true underlying TV interactions in both the time and frequency domains. We applied our methodology to track time-varying physiological signal couplings during an acute exercise paradigm with excellent time resolution using data collected from healthy young and elderly subjects as well as stroke survivors. The proposed framework can be applied, possibly in real time, to several related biomedical applications whereby continuous physiological monitoring is required (intensive care unit, wearable devices etc.). An interesting extension of our methodology could be the state-space representation of the MVAR model [82], [83], whereby the process noise variance is tracked online, leading to less biased and more robust parameter estimates.

References

[1] G. Buzsáki and A. Draguhn, "Neuronal oscillations in cortical networks," *Science (80-.).*, vol. 304, no. 5679, pp. 1926–1929, 2004.
[2] R. Eckhorn *et al.*, "Coherent oscillations: A mechanism of feature linking in the visual cortex?," *Biol. Cybern.*, vol. 60, no. 2, pp. 121–130, 1988.
[3] P. Fries, "A mechanism for cognitive dynamics: neuronal communication through neuronal coherence," *Trends Cogn. Sci.*, vol. 9, no. 10, pp. 474–480, 2005.
[4] T. H. Bullock *et al.*, "Temporal fluctuations in coherence of brain waves," *Proc. Natl. Acad. Sci.*, vol. 92, no. 25, pp. 11568–11572, 1995.
[5] A. Schnitzler and J. Gross, "Normal and pathological oscillatory communication in the brain," *Nat. Rev. Neurosci.*, vol. 6, no. 4, pp. 285–296, 2005.

This article has been accepted for publication in a future issue of this journal, but has not been fully edited. Content may change prior to final publication. Citation information: DOI 10.1109/TBME.2019.2903012, IEEE Transactions on Biomedical Engineering

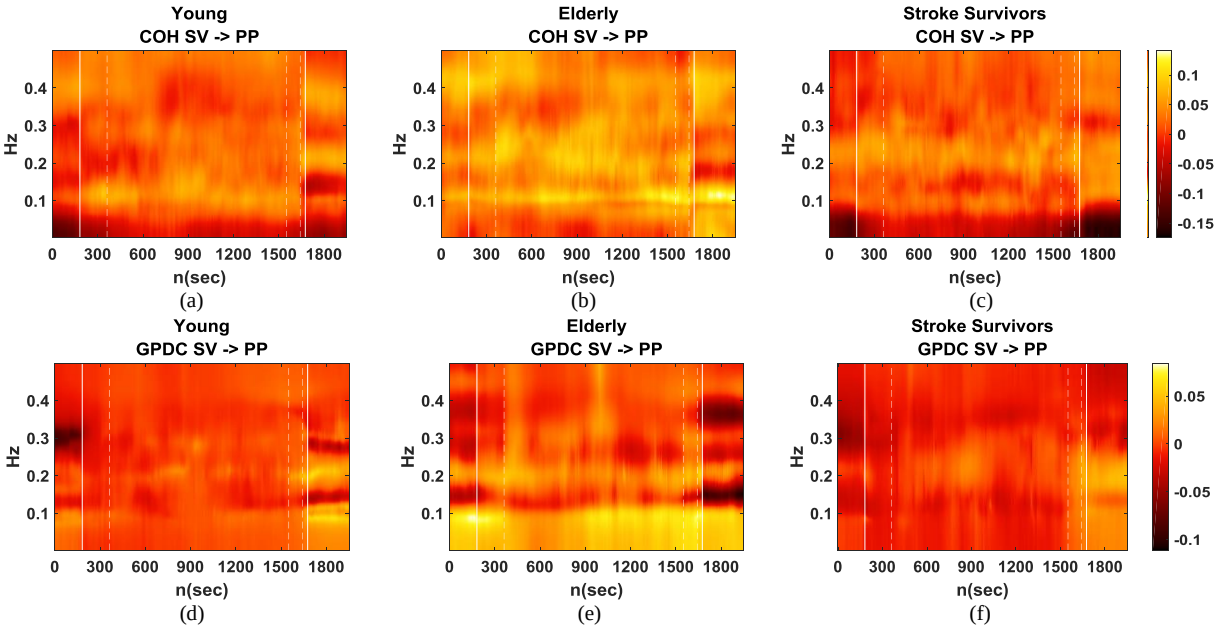

Figure 7: Difference between the median (a,b,c) TV COH of SV and PP and (d,e,f) $GPDC$ from SV to PP estimated using the conventional KF without taking into account heteroskedasticity and the proposed KF combined with the GARCH approach from (a,d) young, (b,e) elderly and (c,f) stroke survivors. The solid white lines denote the onset and offset of the cycling phase (onset of Phases 2 and 6). Dashed white lines denote transition phases. Note that negative values refer to the case where the MVAR measures estimated using the conventional KF (without taking into account heteroskedasticity) have smaller values compared to the ones obtained using the proposed KF combined with the GARCH approach and vice versa. For example, in (d) the HF component of GPDC in young is less pronounced during baseline using the conventional KF compared to the proposed KF combined with the GARCH approach.

[6] T. Mima and M. Hallett, "Corticomuscular coherence: a review," *J. Clin. Neurophysiol.*, vol. 16, no. 6, p. 501, 1999.

[7] M. G. Rosenblum, L. Cimponeriu, A. Bezerianos, A. Patzak, and R. Mrowka, "Identification of coupling direction: application to cardiorespiratory interaction," *Phys. Rev. E*, vol. 65, no. 4, p. 41909, 2002.

[8] S. Cerutti *et al.*, "Time-frequency and time-varying analysis for assessing the dynamic responses of cardiovascular control," *Crit. Rev. Biomed. Eng.*, vol. 30, no. 1–3, 2002.

[9] L. Faes *et al.*, "Causal transfer function analysis to describe closed loop interactions between cardiovascular and cardiorespiratory variability signals," *Biol. Cybern.*, vol. 90, no. 6, pp. 390–399, 2004.

[10] H. Lütkepohl, *New introduction to multiple time series analysis*. Springer Science & Business Media, 2005.

[11] M. J. Kaminski and K. J. Blinowska, "A new method of the description of the information flow in the brain structures," *Biol. Cybern.*, vol. 65, no. 3, pp. 203–210, 1991.

[12] C. W. Anderson *et al.*, "Multivariate autoregressive models for classification of spontaneous electroencephalographic signals during mental tasks," *IEEE Trans. Biomed. Eng.*, vol. 45, no. 3, pp. 277–286, 1998.

[13] L. Faes *et al.*, "Testing Frequency-Domain Causality in Multivariate Time Series," vol. 57, no. 8, pp. 1897–1906, 2010.

[14] T. Milde *et al.*, "NeuroImage A new Kalman fi lter approach for the estimation of high-dimensional time-variant multivariate AR models and its application in analysis of laser-evoked brain potentials," vol. 50, pp. 960–969, 2010.

[15] A. H. Omidvarnia *et al.*, "Kalman filter-based time-varying cortical connectivity analysis of newborn EEG," in *Engineering in Medicine and Biology Society, EMBC, 2011 Annual International Conference of the IEEE*, 2011, pp. 1423–1426.

[16] L. Hu *et al.*, "A time-varying source connectivity approach to reveal human somatosensory information processing," *Neuroimage*, vol. 62, pp. 217–228, 2012.

[17] P. L. C. Rodrigues and L. A. Baccalá, "Statistically significant time-varying neural connectivity estimation using generalized partial directed coherence," in *Engineering in Medicine and Biology Society (EMBC), 2016 IEEE 38th Annual International Conference of the*, 2016, pp. 5493–5496.

[18] J. O. Garcia *et al.*, "Estimating direction in brain-behavior interactions: Proactive and reactive brain states in driving," *Neuroimage*, vol. 150, pp. 239–249, 2017.

[19] M. F. Pagnotta and G. Plomp, "Time-varying MVAR algorithms for directed connectivity analysis: Critical comparison in simulations and benchmark EEG data," *PLoS One*, vol. 13, no. 6, p. e0198846, 2018.

[20] M. Ding *et al.*, "Short-window spectral analysis of cortical event-related potentials by adaptive multivariate autoregressive modeling: data preprocessing, model validation, and variability assessment," *Biol. Cybern.*, vol. 83, no. 1, pp. 35–45, 2000.

[21] E. Möller *et al.*, "Instantaneous multivariate EEG coherence analysis by means of adaptive high-dimensional autoregressive models," *J. Neurosci. Methods*, vol. 105, no. 2, pp. 143–158, 2001.

[22] R. Kus *et al.*, "Determination of EEG activity propagation: pair-wise versus multichannel estimate," *IEEE Trans. Biomed. Eng.*, vol. 51, no. 9, pp. 1501–1510, 2004.

[23] F. Babiloni *et al.*, "Estimation of the cortical functional connectivity with the multimodal integration of high-resolution EEG and fMRI data by directed transfer function," *Neuroimage*, vol. 24, no. 1, pp. 118–131, 2005.

[24] L. Astolfi *et al.*, "Estimation of the time-varying cortical connectivity patterns by the adaptive multivariate estimators in high resolution EEG studies," in *Engineering in Medicine and Biology Society, 2006. EMBS'06. 28th Annual International Conference of the IEEE*, 2006, pp. 2446–2449.

[25] L. Astolfi *et al.*, "Comparison of different cortical connectivity estimators for high-resolution EEG recordings," *Hum. Brain Mapp.*, vol. 28, no. 2, pp. 143–157, 2007.

[26] C. Wilke *et al.*, "Estimation of time-varying connectivity patterns through the use of an adaptive directed transfer function," *IEEE Trans. Biomed. Eng.*, vol. 55, no. 11, pp. 2557–2564, 2008.

[27] L. Astolfi *et al.*, "Tracking the time-varying cortical connectivity patterns by adaptive multivariate estimators," *IEEE Trans. Biomed. Eng.*, vol. 55, no. 3, pp. 902–913, 2008.

[28] G. Baselli *et al.*, "Spectral and cross-spectral analysis of heart rate and arterial blood pressure variability signals," *Comput. Biomed. Res.*, vol. 19, no. 6, pp. 520–534, 1986.

[29] G. Baselli *et al.*, "Spectral decomposition in multichannel recordings based on multivariate parametric identification," *IEEE Trans. Biomed. Eng.*, vol. 44, no. 11, pp. 1092–1101, 1997.

[30] L. T. Mainardi *et al.*, "Multivariate time-variant identification of cardiovascular variability signals: a beat-to-beat spectral parameter estimation in vasovagal syncope," *IEEE Trans. Biomed. Eng.*, vol. 44, no. 10, pp. 978–989, 1997.

[31] R. Barbieri *et al.*, "Multivariate time-variant autoregressive techniques

for closed-loop cardiovascular control using simulations and comparisons," *Stud. Health Technol. Inform.*, pp. 101–114, 1997.

[32] R. Barbieri *et al.*, "Closed-versus open-loop assessment of heart rate baroreflex," *IEEE Eng. Med. Biol. Mag.*, vol. 20, no. 2, pp. 33–42, 2001.

[33] A. Porta, R. Furlan *et al.*, "Quantifying the strength of the linear causal coupling in closed loop interacting cardiovascular variability signals," *Biol. Cybern.*, vol. 86, no. 3, pp. 241–251, 2002.

[34] L. Faes *et al.*, "Causal cross-spectral analysis of heart rate and blood pressure variability for describing the impairment of the cardiovascular control in neurally mediated syncope," *IEEE Trans. Biomed. Eng.*, vol. 53, no. 1, pp. 65–73, 2006.

[35] V. Müller and U. Lindenberger, "Cardiac and respiratory patterns synchronize between persons during choir singing," *PLoS One*, vol. 6, no. 9, p. e24893, 2011.

[36] A. Porta *et al.*, "Accounting for respiration is necessary to reliably infer Granger causality from cardiovascular variability series," *IEEE Trans. Biomed. Eng.*, vol. 59, no. 3, pp. 832–841, 2012.

[37] M. Niedzwiecki, *Identification of Time-varying Processes*. John Wiley & Sons, Ltd, 2000.

[38] T. Milde *et al.*, "A new Kalman filter approach for the estimation of high-dimensional time-variant multivariate AR models and its application in analysis of laser-evoked brain potentials," *Neuroimage*, vol. 50, no. 3, pp. 960–969, 2010.

[39] E. Möller *et al.*, "Instantaneous multivariate EEG coherence analysis by means of adaptive high-dimensional autoregressive models," *J. Neurosci. Methods*, vol. 105, pp. 143–158, 2001.

[40] D. Lawrence *et al.*, "Handbook of genetic algorithms," *Van No Strand Reinhold, New York*, 1991.

[41] K. Deb, "An efficient constraint handling method for genetic algorithms," *Comput. Methods Appl. Mech. Eng.*, vol. 186, no. 2–4, pp. 311–338, 2000.

[42] K. Kostoglou *et al.*, "Modeling of multiple-input, time-varying nonlinear systems with recursively estimated basis expansions," *Submitt. to IEEE Trans. Signal Process.*, 2017.

[43] H. Akaike, "A new look at the statistical model identification," *{IEEE} Trans. Autom. Control*, vol. 19, no. 6, pp. 716–723, 1974.

[44] A. Omidvarnia *et al.*, "Measuring time-varying information flow in scalp EEG signals: orthogonalized partial directed coherence," *IEEE Trans. Biomed. Eng.*, vol. 61, no. 3, pp. 680–693, 2014.

[45] S. De Waele and P. M. T. Broersen, "Order Selection for Vector Autoregressive Models," vol. 51, no. 2, pp. 427–433, 2003.

[46] L. Faes *et al.*, "Measuring connectivity in linear multivariate processes: definitions, interpretation, and practical analysis," *Comput. Math. Methods Med.*, vol. 2012, 2012.

[47] H. E. Rauch *et al.*, "Maximum likelihood estimates of linear dynamic systems," *AIAA J.*, vol. 3, no. 8, pp. 1445–1450, 1965.

[48] M. P. Tarvainen *et al.fsupll*, "Estimation of Nonstationary EEG With Kalman Smoother Approach : An Application to Event- Estimation of Nonstationary EEG With Kalman Smoother Approach : An Application to," no. April, 2004.

[49] S. M. Kay, *Modern spectral estimation*. Pearson Education India, 1988.

[50] L. A. Baccala *et al.*, "Studying the interaction between brain structures via directed coherence and Granger causality," *Appl. Signal Process.*, vol. 5, no. 1, p. 40, 1998.

[51] K. Yacoub, "Relationship between multiple and partial coherence functions," *IEEE Trans. Inf. Theory*, vol. 16, no. 6, pp. 668–672, 1970.

[52] M. Eichler *et al.*, "Partial correlation analysis for the identification of synaptic connections," *Biol. Cybern.*, vol. 89, no. 4, pp. 289–302, 2003.

[53] L. A. Baccalá *et al.*, "Generalized partial directed coherence," in *2007 15th International Conference on Digital Signal Processing*, 2007, pp. 163–166.

[54] T. Bollerslev, "Generalized autoregressive conditional heteroskedasticity," *J. Econom.*, vol. 31, no. 3, pp. 307–327, 1986.

[55] P. Kovesi, "Good colour maps: How to design them," *arXiv Prepr. arXiv1509.03700*, 2015.

[56] A. D. Robertson *et al.*, "Exercise intensity modulates the change in cerebral blood flow following aerobic exercise in chronic stroke," *Exp. brain Res.*, vol. 233, no. 8, pp. 2467–2475, 2015.

[57] B. J. MacIntosh *et al.*, "Impact of a single bout of aerobic exercise on regional brain perfusion and activation responses in healthy young adults.," *PLoS One*, vol. 9, no. 1, p. e85163, 2014.

[58] A. S. Rajab *et al.*, "A single session of exercise increases connectivity in sensorimotor-related brain networks: a resting-state fMRI study in young healthy adults," *Front. Hum. Neurosci.*, vol. 8, 2014.

[59] D. Chemla *et al.*, "Total arterial compliance estimated by stroke volume-to-aortic pulse pressure ratio in humans," *Am. J. Physiol. Circ. Physiol.*, vol. 274, no. 2, pp. H500--H505, 1998.

[60] G. de Simone *et al.*, "Stroke volume/pulse pressure ratio and cardiovascular risk in arterial hypertension," *Hypertension*, vol. 33, no. 3, pp. 800–805, 1999.

[61] A. W. Ashor *et al.*, "Effects of exercise modalities on arterial stiffness and wave reflection: a systematic review and meta-analysis of randomized controlled trials," *PLoS One*, vol. 9, no. 10, p. e110034, 2014.

[62] T. Okamoto *et al.*, "Arterial compliance and stiffness following low-intensity resistance exercise," *Eur. J. Appl. Physiol.*, vol. 114, no. 2, pp. 235–241, 2014.

[63] H. Kawano *et al.*, "Resistance training and arterial compliance: keeping the benefits while minimizing the stiffening," *J. Hypertens.*, vol. 24, no. 9, pp. 1753–1759, 2006.

[64] B. A. Kingwell *et al.*, "Arterial compliance increases after moderate-intensity cycling," *Am. J. Physiol. Circ. Physiol.*, vol. 273, no. 5, pp. H2186--H2191, 1997.

[65] A. E. DeVan *et al.*, "Acute effects of resistance exercise on arterial compliance," *J. Appl. Physiol.*, vol. 98, no. 6, pp. 2287–2291, 2005.

[66] H. Tanaka *et al.*, "Aging, habitual exercise, and dynamic arterial compliance," *Circulation*, vol. 102, no. 11, pp. 1270–1275, 2000.

[67] R. Zhang *et al.*, "Spontaneous fluctuations in cerebral blood flow: insights from extended-duration recordings in humans," *Am. J. Physiol. Circ. Physiol.*, vol. 278, no. 6, pp. H1848--H1855, 2000.

[68] T. Otsuki *et al.*, "Contribution of systemic arterial compliance and systemic vascular resistance to effective arterial elastance changes during exercise in humans," *Acta Physiol.*, vol. 188, no. 1, pp. 15–20, 2006.

[69] Z. Zhao *et al.*, "Spectral and Coherence Analysis of the Variabilities of Heart Rate, Stroke Volume, and Systolic Blood Pressure in Exercise Stress Tests," vol. 25, no. Bhi, pp. 771–774, 2012.

[70] R. Perini and A. Veicsteinas, "Heart rate variability and autonomic activity at rest and during exercise in various physiological conditions," *Eur. J. Appl. Physiol.*, vol. 90, no. 3–4, pp. 317–325, 2003.

[71] J. Sung *et al.*, "The relationship between arterial stiffness and increase in blood pressure during exercise in normotensive persons," *J. Hypertens.*, vol. 30, no. 3, pp. 587–591, 2012.

[72] S. S. Franklin, "Ageing and hypertension: the assessment of blood pressure indices in predicting coronary heart disease.," *J. Hypertens. Suppl. Off. J. Int. Soc. Hypertens.*, vol. 17, no. 5, pp. S29--36, 1999.

[73] M. E. Safar *et al.*, "Current perspectives on arterial stiffness and pulse pressure in hypertension and cardiovascular diseases," *Circulation*, vol. 107, no. 22, pp. 2864–2869, 2003.

[74] M. Javorka *et al.*, "Causal coherence analysis of cardiovascular variables in obese preadolescents and adolescents," in *Engineering in Medicine and Biology Society (EMBC), 2015 37th Annual International Conference of the IEEE*, 2015, pp. 1793–1796.

[75] A. J. Camm *et al.*, "Heart rate variability: standards of measurement, physiological interpretation and clinical use. Task Force of the European Society of Cardiology and the North American Society of Pacing and Electrophysiology," *Circulation*, vol. 93, no. 5, pp. 1043–1065, 1996.

[76] G. E. Billman, "Heart rate variability--a historical perspective," *Front. Physiol.*, vol. 2, 2011.

[77] A. McLaren *et al.*, "Autonomic function is impaired in elderly stroke survivors," *Stroke*, vol. 36, no. 5, pp. 1026–1030, 2005.

[78] M. Dütsch *et al.*, "Cardiovascular autonomic function in poststroke patients," *Neurology*, vol. 69, no. 24, pp. 2249–2255, 2007.

[79] D. R. Seals and M. D. Esler, "Human ageing and the sympathoadrenal system," *J. Physiol.*, vol. 528, no. 3, pp. 407–417, 2000.

[80] S. Ogoh *et al.*, "Middle cerebral artery flow velocity and pulse pressure during dynamic exercise in humans," *Am J Physiol Hear. Circ Physiol*, vol. 288, no. 4, pp. H1526–H1531, 2005.

[81] J. P. Fisher *et al.*, "Regulation of middle cerebral artery blood velocity during dynamic exercise in humans: influence of aging," *J. Appl. Physiol.*, vol. 105, no. 1, pp. 266–273, 2008.

[82] L. Faes *et al.*, "Multiscale Granger causality," *Phys. Rev. E*, vol. 96, no. 4, pp. 1–7, 2017.

[83] L. Faes *et al.*, "On the interpretability and computational reliability of frequency-domain Granger causality," *F1000Research*, vol. 6, 2017.